Characterization of Moisture Content in a Concrete Panel Using Synthetic Aperture Radar Images

Ahmed Alzeyadi, S.M.ASCE[1]; and Tzuyang Yu, Ph.D., A.M.ASCE[2]

Abstract: Moisture content in concrete structures is commonly associated with many durability problems (e.g., steel corrosion and freeze-thaw) and can be used in structural health monitoring and nondestructive testing of concrete structures. In this paper, the use of synthetic aperture radar (SAR) imaging for characterizing subsurface moisture content and distribution is proposed, using a concrete panel specimen as an example. A $0.3 \times 0.3 \times 0.05$-m concrete panel specimen cast and conditioned in laboratory was air-dried for almost 5 months and simultaneously monitored for its moisture variation by SAR imaging. From the analysis of its SAR images at different moisture contents, it was found that SAR images can not only qualitatively capture the moisture distribution inside concrete but can also quantitatively correlate with the overall moisture content inside concrete. Higher SAR amplitudes indicate stronger electromagnetic scattering response, suggesting greater values of dielectric constant. A critical contour in SAR images is proposed as an insightful measure for the subsurface sensing of concrete. An approach for determining the critical contour in each SAR image is proposed. **DOI: 10.1061/(ASCE)AS.1943-5525.0000945.**
© 2018 American Society of Civil Engineers.

Downloaded from ascelibrary.org by Tzuyang Yu on 09/11/18. Copyright ASCE. For personal use only; all rights reserved.

Introduction

Presence of moisture inside portland cement concrete plays a significant role in short-term strength development (cement hydration) and long-term durability of reinforced and prestressed concrete structures. Moisture inside concrete not only facilitates most durability problems [e.g., freezing and thawing (Wang et al. 2014; Zeng et al. 2011; Cai and Liu 1998), steel reinforcement corrosion, carbonation, and alkali-silica reaction (ASR)] in concrete structures, but its amount and distribution are also related to the hydraulic permeability of concrete. In the freeze-thaw damage of non-air-entrained concrete, it has been reported that concrete will experience significant damage when its moisture content exceeds 80% (Fagerlund 1977). In the chloride-induced corrosion of steel rebar inside concrete structures, moisture facilitates the diffusion of water through the capillary pores inside concrete (Gonzalez et al. 1993; Bentur et al. 1997). Carbonation of concrete is encouraged when the relative humidity inside concrete is between 55%–65% (Gonzalez et al. 1993). Research has also shown that expansive ASR can occur in concrete having a relative humidity above 80% (Stark 1991). In addition, it is well known that saturated concrete is weaker than dry concrete, generally by 20% (Shoukry et al. 2011; Li et al. 2009).

Despite knowing that moisture content in concrete is crucial to the performance of concrete structures, it is difficult to determine the moisture content inside concrete in the field without using intrusive or embedded moisture sensors. To avoid troublesome issues associated with embedded moisture sensors, nondestructive evaluation/testing (NDE/T) techniques have been applied. Among existing NDE/T techniques, gravimetric sensors (Akita et al. 1997; Šelih et al. 1996), gamma densitometry (Multon et al. 2004; Amba et al. 2010), relative humidity, and thermal and microwave/radar methods (Sbartaï et al. 2006, 2007) have been applied for moisture determination. In general, an ideal NDE/T technique for moisture determination in concrete must be quantitative, capable of detecting internal moisture distribution, and invulnerable to environmental factors [e.g., temperature and soluble salt content (Cornell and Coote 1972)]. Ultimately, it has been suggested that such a technique should be able to quantify different phases (free water, bound water, and chemically bound water) of moisture inside concrete (Quincot et al. 2011).

Electromagnetic techniques such as ground-penetrating radar (GPR), on the other hand, are capable of conducting spatial and quantitative moisture determination in concrete specimens (Sbartaï et al. 2006; Senin and Hamid 2016; Sbartaï et al. 2007; Yu 2010, 2011) and structures (Chen and Wimsatt 2010; Yu 2017). The ability of radar signals (electromagnetic waves) to propagate through dielectrics like concrete makes electromagnetic techniques suitable for conducting subsurface moisture content measurements inside concrete. Laurens et al. (2002) used a 1.5-GHz central frequency GPR system to evaluate the moisture content of $0.5 \times 0.5 \times 0.07$-m concrete slabs at various saturation levels (0%–100%). They found that the GPR signal attenuates linearly with increases of moisture content. It was also reported that the presence of moisture reduces the center frequency of reflected GPR signal in another similar study (Laurens et al. 2005). Sbartaï et al. (2006) studied the amplitudes of GPR signals (direct and reflected) with a center frequency of 1.5 GHz inside concrete slabs ($0.75 \times 0.5 \times 0.08$ m) at different moisture levels (0%, 20%, 40%, 60%, 80%, and 100%). They also found that amplitudes of direct and reflected GPR signals decrease linearly with the increase in moisture content. Klysz and Balayssac (2007) applied a GPR (300–1,200 MHz) system on concrete slabs ($0.6 \times 0.6 \times 0.12$ m) with various moisture contents to investigate the effect of moisture on GPR signal amplitude and signal velocity. They found that both amplitude and velocity of the GPR signal reduce with increases in moisture content (an indication of dielectric dispersion). Although most researchers reported linear attenuation of GPR signals with the increase of moisture content in

[1]Doctoral Candidate, Dept. of Civil and Environmental Engineering, Univ. of Massachusetts Lowell, Lowell, MA 01854. Email: Ahmed_AlZeyadi@student.uml.edu

[2]Associate Professor, Dept. of Civil and Environmental Engineering, Univ. of Massachusetts Lowell, Lowell, MA 01854 (corresponding author). Email: Tzuyang_Yu@uml.edu

Note. This manuscript was submitted on February 8, 2018; approved on June 4, 2018; published online on September 11, 2018. Discussion period open until February 11, 2019; separate discussions must be submitted for individual papers. This paper is part of the ***Journal of Aerospace Engineering***, © ASCE, ISSN 0893-1321.

concrete, some reported a nonlinear attenuation between GPR signal and moisture content (Sbartaï et al. 2009). A literature review revealed that there are no other reported radar imaging techniques besides GPR for the determination of moisture content in concrete.

The objective of this paper is to apply synthetic aperture radar (SAR) imaging for determining moisture content in concrete specimens. SAR imaging is a relatively new technique in civil engineering applications. Unlike GPR, SAR imaging utilizes image superposition to improve resolution and damage detectability. In this paper, the principle of SAR imaging is first introduced, followed by the experimental work on specimen preparation, moisture monitoring, and laboratory SAR imaging. Research findings are summarized and finally, conclusions are offered.

Principle of SAR Imaging

In SAR imaging, high-resolution coherent images are produced with adjustable frequency bandwidth and radar aperture. Higher frequencies and wider bandwidths lead to SAR images with better resolution, and the increased radar aperture due to prolonged radar movement can also produce high-resolution SAR images. An image-formation algorithm is used to produce such coherent images from raw SAR data. In SAR imaging, the back-scattering pattern of any target is first formulated by a planar scattering problem in a domain Ω_s containing N scattering points (Fig. 1). Consider an incident wave with unit amplitude as follows (Kong 2000):

$$\psi_{\text{inc}}(\bar{r}) = \frac{1}{r} \cdot \exp(i\bar{k}_i \cdot \bar{r}) \tag{1}$$

where $\bar{k}_i = k_{ix}\hat{x} - k_{ix}\hat{y}$ is the incident wave vector; and $\bar{r}$ is the position vector from the radar to any observation point, $|\bar{r}| = r$. The scattered field from scatterer j at $\bar{r}_j$ and observed at $\bar{r}$ is (Tsang et al. 2000)

$$\psi_{\text{scat}}(\bar{r}, \bar{r}_j) = \frac{s_j(\bar{r}, \hat{k}_i)}{|\bar{r} - \bar{r}_j|} \cdot \exp(ik|\bar{r} - \bar{r}_j|) \cdot \psi_{\text{inc}}(\bar{r}) \tag{2}$$

where $s_j = s_j(\bar{r}, \hat{k}_i)$ is the scattered amplitude at scatterer j due to an incident wave at $\hat{k}_i$ and observed at $\bar{r}$; $i = \sqrt{-1}$; and $k = \omega/c$. By neglecting the higher-order interactions among scatterers in this formulation, the total scattered field from N scatterers observed at $\bar{r}$ is the summation of all the scattered fields, as follows:

$$\psi_{\text{scat}}(\bar{r}) = \sum_{j=1}^{N} \frac{s_j(\bar{r}, \hat{k}_i)}{|\bar{r} - \bar{r}_j|} \cdot \exp(ik|\bar{r} - \bar{r}_j|) \cdot \psi_{\text{inc}}(\bar{r}) \tag{3}$$

where $\bar{k}_s = k_{sx}\hat{x} + k_{sy}\hat{y}$ is the scattering direction vector, where $\bar{k}_s = -\bar{k}_i$ when the radar operates in monostatic mode. Considering

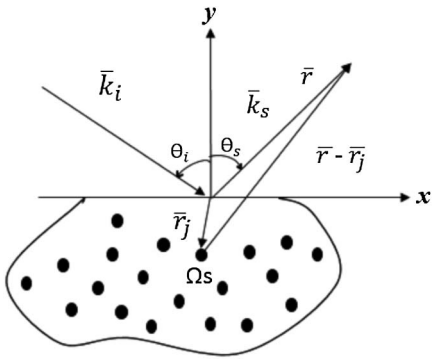

Fig. 1. N point scattering domain.

the case of a single scatterer without losing generality, Eq. (3) can be written

$$\psi_{\text{scat}}(\omega, \theta) = \psi_{\text{scat}}(k, \bar{r}_s) = \frac{s_\theta}{r^2} \cdot \exp\left[i\frac{r}{c}\omega(1 + \cos^2\theta - \sin^2\theta)\right] \tag{4}$$

where $\theta = \theta_i = \tan^{-1}(k_{iy}/k_{ix})$. Eq. (4) is obtained by taking a slice of the two-dimensional (2D) Fourier transform (FT) of the domain Ω_s.

In other reconstruction algorithms, all projections are superimposed before 2D inverse fourier transform (IFT) (plane projection) is carried out to obtain the final image. However, in the back-projection algorithm, one-dimensional (1D) IFT is performed first to generate subimages. The final image is obtained by summing up all subimages. A frequency modulation operator (or time-domain convolution operator) is applied to ensure that the center in back-projection images coincides with the center of the scatterer. A shifting-back step in the back-projection algorithm in the frequency domain is performed by applying a ramp filter in which frequency ω_n is shifted back by a carrier frequency ω_c

$$\begin{aligned} P(\nu, \theta) &= \int_{\omega_{\min}}^{\omega_{\max}} d\omega \cdot \psi_{\text{scat}}(\omega - \omega_c, \theta)|\omega - \omega_c| \cdot \exp(-i\omega\nu) \\ &= \frac{s_\theta}{r^2} \cdot \int_{\omega_{\min}}^{\omega_{\max}} d\omega \cdot |\omega - \omega_c| \\ &\quad \cdot \exp\left[i\frac{r}{c}(\omega - \omega_c) \times (1 + \cos^2\theta - \sin^2\theta) - i\omega\nu\right] \end{aligned} \tag{5}$$

where ν = spatial variable of the 1D IFT projection. Translating the local 1D IFT coordinate $[\nu, P(\nu, \theta_s)]$ to the global polar coordinate (r, ϕ) indicates that

$$\nu = r\cos(\phi - \theta_s) \tag{6}$$

Upsampling is required when transforming from $P(\nu, \theta)$ to $P[r\cos(\phi - \theta), \theta]$ to ensure the quality of back-projection images. In other words, $P[r\cos(\phi - \theta), \theta]$ is obtained by interpolating $P(\nu, \theta)$. In the polar coordinate system, a back-projection image is finally obtained by integrating subimages at various azimuth angles over the entire inspection range

$$\begin{aligned} I(r, \phi) &= \int_{-\theta_{\text{int}/2}}^{\theta_{\text{int}/2}} d\theta \cdot P(r\cos(\phi - \theta), \theta) \\ &= \frac{s_\theta}{r^2} \cdot \int_{-\theta_{\text{int}/2}}^{\theta_{\text{int}/2}} d\theta \int_{\omega_{\min}}^{\omega_{\max}} d\omega \cdot |\omega - \omega_c| \\ &\quad \cdot \exp\left[i\frac{r}{c}(\omega - \omega_c) \cdot (1 + \cos^2\theta - \sin^2\theta) - i\omega r\cos(\phi - \theta_s)\right] \end{aligned} \tag{7}$$

where the polar coordinates (r, ϕ) are related to the Cartesian coordinates by

$$x = r\cos\phi \tag{8}$$

$$y = r\sin\phi \tag{9}$$

Therefore, the image plane $I(x, y) = I(r\cos\phi, r\sin\phi)$ can be reconstructed. Fig. 2 illustrates the processing step of the back-projection algorithm.

Downloaded from ascelibrary.org by Tzuyang Yu on 09/11/18. Copyright ASCE. For personal use only; all rights reserved.

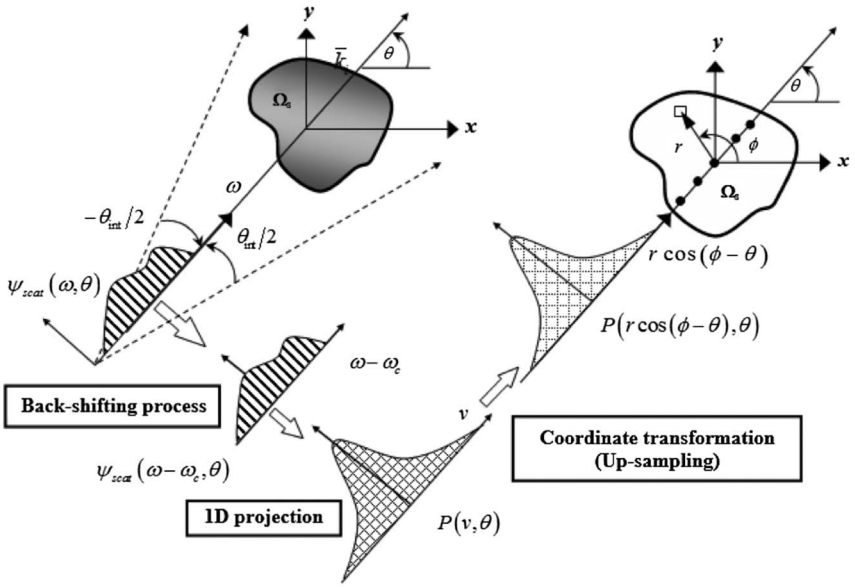

Fig. 2. Back-projection algorithm processing steps.

Experimental Program

Specimen Preparation

A $0.3 \times 0.3 \times 0.05$-m concrete panel was designed and manufactured for the purpose of moisture characterization inside concrete. General-purpose Type I/II portland cement was used. The mix design ratio (by weight) was 1:2:4 for cement: fine aggregate: coarse aggregate. The concrete panel was moist-cured for 28 days and stored in room conditions (air-drying) for almost 5 months. Table 1 lists the design information of the concrete panel. Fig. 3 shows a picture and schematic diagram of the concrete panel.

Table 1. Design of concrete panel

Property	Value
w/c ratio	0.45
Mix ratio	1:2:4
Maximum coarse aggregate size (cm)	2.50
Minimum coarse aggregate size (cm)	0.90

Note: w/c ratio = water-to-cement ratio.

Moisture Monitoring

During the SAR imaging process, the mass of the panel was monitored using an electronic scale for almost 5 months. After the moisture monitoring period, the panel was oven-heated at an elevated temperature of 80°C for 1 month (30 days) until the mass stabilized. The last mass measurement was used as the zero-moisture mass of the concrete panel. The moisture content of concrete panel was calculated by

$$\psi = \frac{m_w - m_d}{m_d} \cdot 100 \tag{10}$$

where ψ = moisture content (%); m_w = mass of concrete panel at a given air-drying time; and m_d = oven-dried mass of concrete panel at the end of the oven-heating period.

SAR Imaging

SAR images of the concrete panel at various moisture contents were conducted using a 10-GHz continuous-wave imaging radar (CWIR) system with a 1.5-GHz bandwidth inside an anechoic chamber at the Electromagnetic Remote Sensing Laboratory at

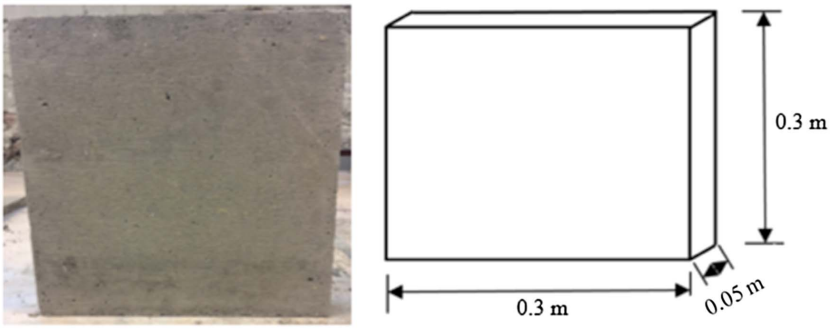

(a) (b)

Fig. 3. (a) Picture; and (b) schematic of concrete panel.

J. Aerosp. Eng., 2019, 32(1): 04018112

Downloaded from ascelibrary.org by Tzuyang Yu on 09/11/18. Copyright ASCE. For personal use only; all rights reserved.

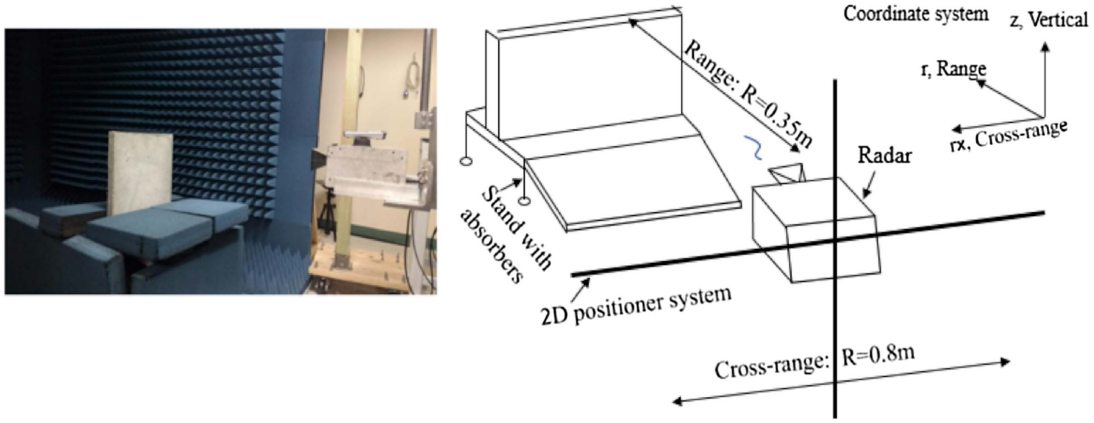

Fig. 4. (a) Picture; and (b) schematic of SAR imaging system.

the University of Massachusetts at Lowell. The CWIR system operates in the stripmap SAR mode by using a 2D positioner. In all SAR images, the range (r) of the concrete panel was 0.35 m and the cross range $r_x = 0.80$ m. SAR images were collected at different moisture contents in the same experimental configuration. Fig. 4 shows a picture and schematic setup of the SAR imaging system.

Results and Findings

Moisture Content Quantification

Fig. 5 shows the time-dependent pattern of the air-dried concrete panel. Average temperature in the laboratory was observed 28°C (Fig. 5). It was found that, in the room-condition (oven-drying) environment, the moisture content of concrete panel decreased rapidly at the early age (0–500 h) at a rate of 0.25% per hour. At the later stage (500–3,219 h), it lost 0.03% of moisture per hour. The rate of moisture loss during 0–500 h was more than eight times the rate during 500–3,219 h. Eq. (11) provides the time-dependent moisture variation model from curve-fitting. The R^2 of the model was 0.9953

$$\psi(t) = ae^{bt} + ce^{dt} \tag{11}$$

where ψ = moisture content (%) at time t; t = time (h); $a = 0.996$; $b = -0.006298$; $c = 2.77$; and $d = -0.0001931$. Eq. (11) can be used for quantifying moisture content inside the concrete panel in this research.

SAR Images of Concrete Panel

SAR images of the concrete panel at different moisture contents were collected as shown in Fig. 6. In Fig. 6, the spatial distribution of SAR amplitudes is rendered on the range–cross-range (r, r_x) plane. Higher SAR amplitudes in Fig. 6 indicate a stronger electromagnetic scattering response, suggesting greater values of dielectric constant (real part of relative complex electric permittivity). Because moisture (liquid water) has a dielectric constant of 78–81 and dry concrete has a dielectric constant of 5–15 in the microwave frequency range, it is expected that the presence of moisture inside concrete will increase the dielectric constant of dry concrete. Fig. 6 provides the experimental validation of dielectric mixture theory in wet/moist concrete as a multiphase porous cementitious composite.

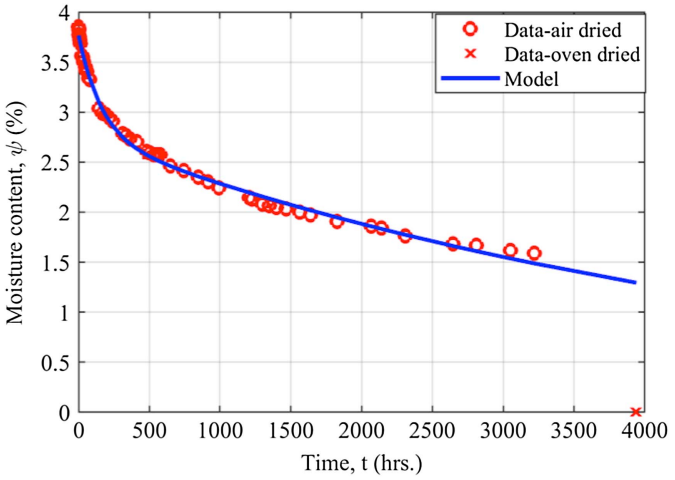

Fig. 5. Moisture content variation with time for the concrete panel.

This result is better illustrated by the slice representation in Fig. 7, taken at a 0.35-m range for selected SAR images.

Spatial Distribution (Shape) of SAR Amplitudes

Furthermore, moisture distribution inside concrete was reconstructed in space by SAR imaging in Fig. 6. As shown in Fig. 6, the shape of SAR amplitudes remained basically constant, except for the oven-dried case ($\psi = 0\%$). Greater SAR amplitudes occupy more area in a SAR image when the concrete panel has higher moisture content. This is because of the stronger electromagnetic reflection from wet concrete, which were integrated by the back-projection algorithm and eventually projected onto the range–cross-range plane. Also, reflection from the back of the concrete panel was not observed for any of the moisture contents except for the oven-dried case. The sensitivity of electromagnetic waves (radar signals) to the change in dielectric properties (moisture content) of concrete enables use of the SAR imaging technique for moisture characterization. This result indicates that, with the increase of moisture content, higher SAR amplitudes also demonstrate wider spatial distribution. This result was attributed to the capability of SAR imaging to project scattered radar signals back to their estimated spatial locations. It indicates that the spatial distribution of SAR amplitudes shows insightful information for

Downloaded from ascelibrary.org by Tzuyang Yu on 09/11/18. Copyright ASCE. For personal use only; all rights reserved.

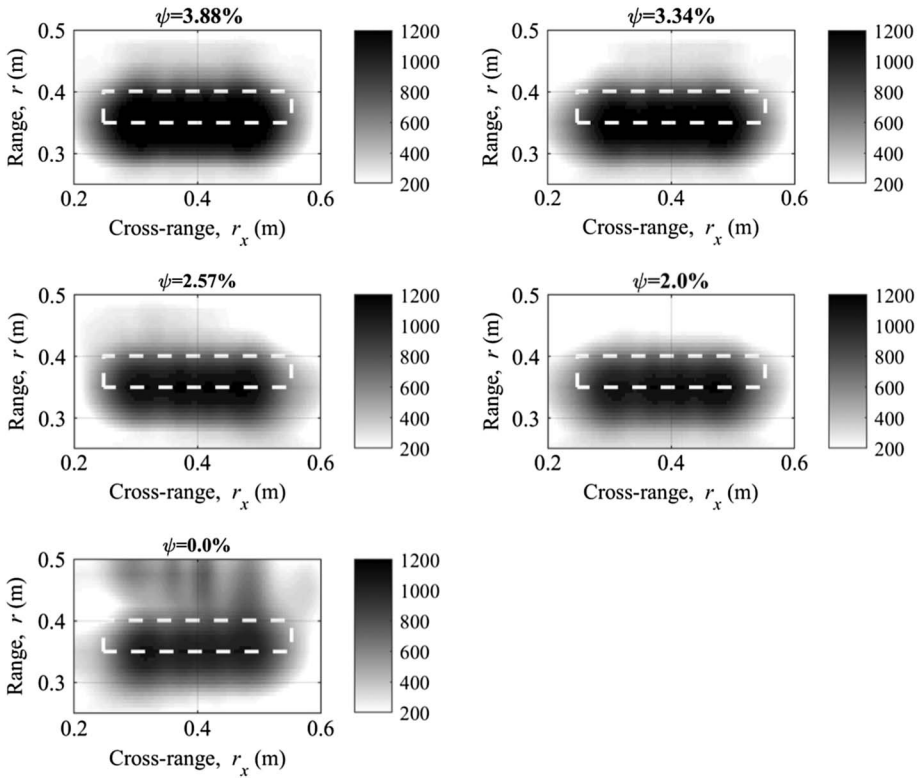

Fig. 6. SAR images of concrete panel at different moisture contents ($\psi = 3.88\% - 0.0\%$).

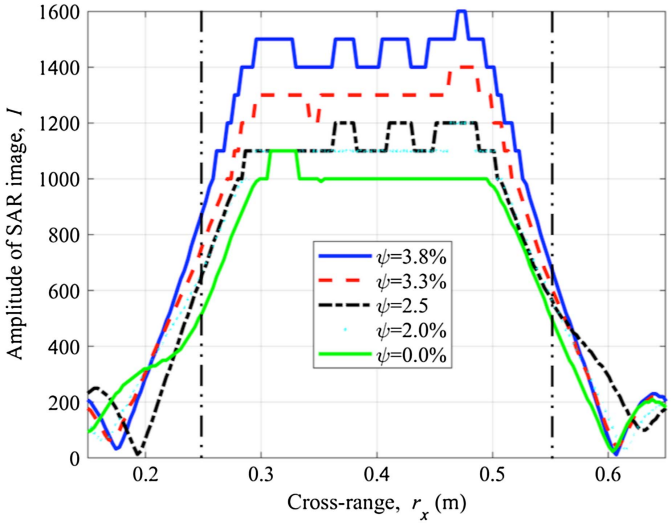

Fig. 7. SAR curves of various moisture contents (0%–3.8%) at 0.35-m range.

subsurface sensing and can be used to relate to the moisture distribution inside a concrete panel specimen.

SAR Image and Its Contour Representation

To better describe the spatial distribution of SAR amplitudes, a critical contour must be selected in order to compare SAR images at different moisture contents. This critical contour will be used as a representative measure to each SAR image. The contour representation also provides an approach to quantify the spatial distribution of SAR amplitudes as a key parameter to estimate moisture distribution inside concrete. Fig. 8 shows an SAR image ($\psi = 3.88\%$) and its contour representation. In Fig. 8, it is clear that each SAR images has many contours from which to choose. In addition, it is evident that the higher the SAR amplitudes, the smaller their size (contour area) and distribution.

To determine the critical contour of each SAR image, optimal SAR amplitude must be used. This optimal SAR amplitude is found by introducing the hypothesis that the change of moisture distribution inside the concrete panel is monotonic in space. Following this hypothesis, when comparing contours representing different moisture contents, there should not be any intersections among contours (monotonic expansion or contraction). In other words, the moisture distribution at a higher level of moisture content will always include the one at a lower level of moisture content. Figs. 9 and 10 show the comparisons of contours using two different SAR amplitudes. It can be seen that in Fig. 9, a monotonic increase of moisture content does not lead to monotonic expansion of contours when choosing SAR amplitude I to be 900. This is the case when there are interactions among contours. On the other hand, when choosing $I = 1{,}000$ in Fig. 10, there is no interaction among contours, suggesting that the choice of $I = 1{,}000$ satisfies the proposed hypothesis. In other words, the optimal SAR amplitude in this experimental work was found to be 1,000. After the optimal SAR amplitude is determined, critical contours and their areas for SAR images at various moisture contents can be found.

Once the optimal SAR amplitude was selected, critical contour area (A_c) could then be calculated from each SAR image. Critical contour areas of SAR images at different moisture contents were determined in Fig. 11 and modeled by Eq. (12)

$$A_c(\psi) = ae^{b\psi} + c \tag{12}$$

where A_c = critical area of contour at $I_c = 1{,}000$; ψ = moisture content (%); $a = 17.76$; $b = 0.6183$; and $c = 32.89$.

J. Aerosp. Eng., 2019, 32(1): 04018112

Downloaded from ascelibrary.org by Tzuyang Yu on 09/11/18. Copyright ASCE. For personal use only; all rights reserved.

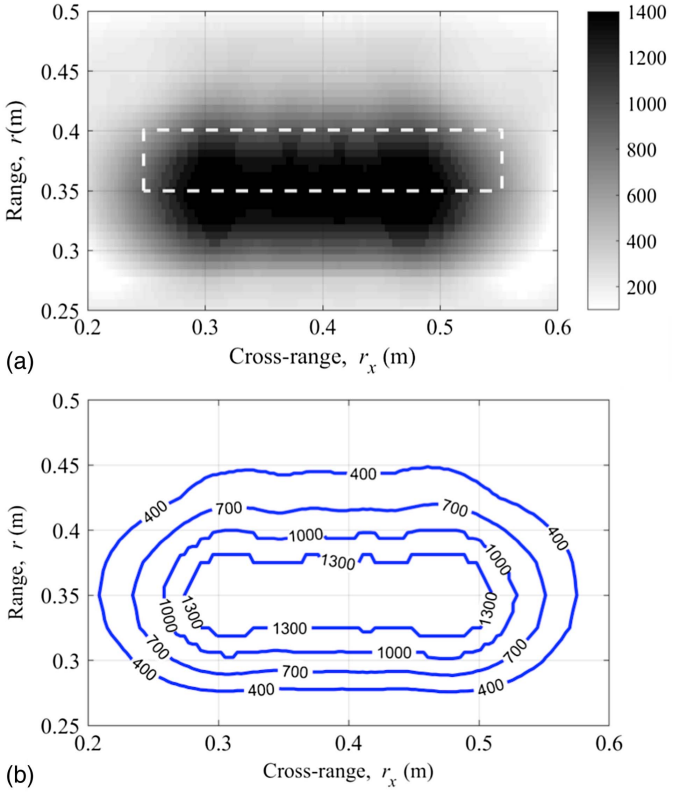

Fig. 8. (a) SAR image at $\psi = 3.88\%$; and (b) its contour representation.

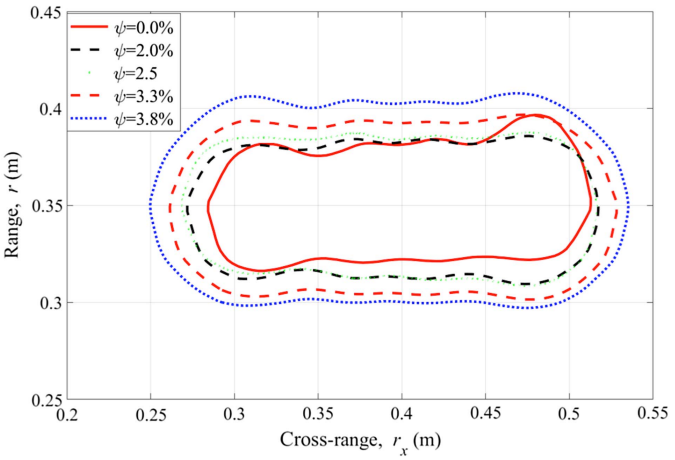

Fig. 9. Comparison of contours for moisture content with $I = 900$.

In summary, it can be seen that critical contours of SAR images qualitatively capture the moisture distribution inside a concrete panel specimen (Fig. 10); in addition, the critical contour area (A_c) can be quantitatively correlated to the overall moisture content of the concrete specimen (Fig. 11) in this research. Steps in the developed approach to characterize moisture content are summarized in Fig. 12.

Discussion of Moisture Distribution

The moisture distribution inside cementitious composites like concrete is instrumental to the inspection and maintenance of concrete structures. Intrusive and nonintrusive techniques have been applied to determining the moisture distribution inside concrete. Intrusive techniques such as embedded moisture sensors (Kim and Lee 1999; Zhang et al. 2009) can directly measure moisture distribution inside concrete specimens, but the presence of sensors can change the

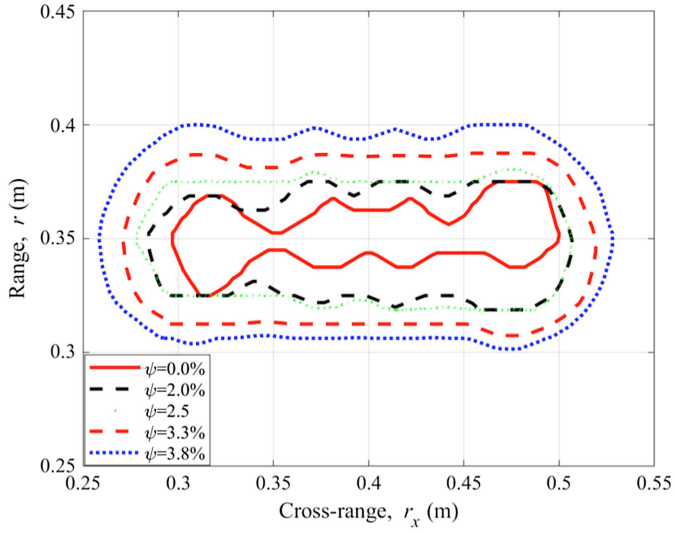

Fig. 10. Comparison of contours for moisture content with $I = 1{,}000$.

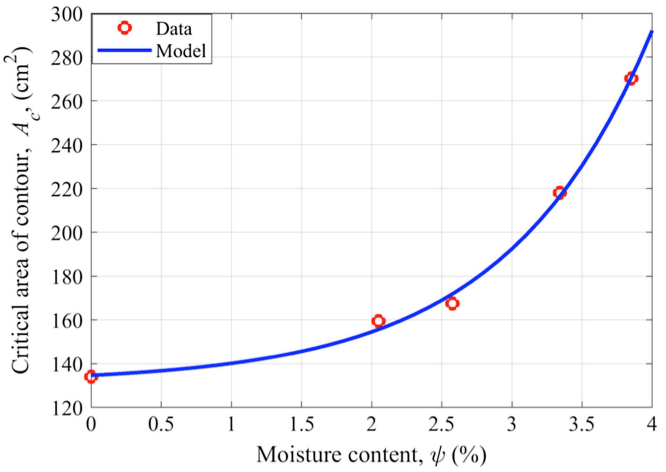

Fig. 11. Critical area of contour at optimal SAR amplitude ($I_c = 1{,}000$) with varying moisture content.

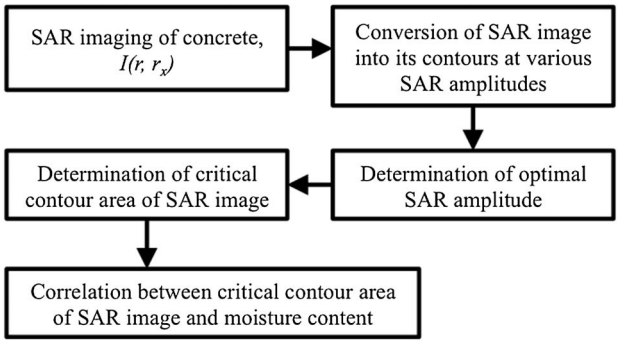

Fig. 12. Procedure of SAR imaging for moisture determination in concrete.

Downloaded from ascelibrary.org by Tzuyang Yu on 09/11/18. Copyright ASCE. For personal use only; all rights reserved.

boundary condition of moisture diffusion in concrete and provide nonrepresentative results. Nonintrusive techniques such as ultrasounds (Popovic 2005), impedance spectroscopy (Sánchez et al. 2013), and magnetic resonance imaging (MRI) signal point imaging (Cano-Barrita et al. 2004) can be applied for concrete specimens prepared in specific shapes and dimensions. From reported data, a double-curvature pattern of moisture distribution has been experimentally confirmed by researchers (Cano-Barrita et al. 2004; Garbalinska et al. 2018). In this double-curvature moisture distribution pattern, subsurface moisture increases slowly from the surface of concrete specimens and increases rapidly to achieve the plateau of the distribution curve after a certain depth.

On the other hand, numerical simulation results using Fick-type diffusion (Garbalinska et al. 2018) and microstructure hydration (Ye et al. 2018) have also been reported to predict the subsurface moisture distribution. These numerical models predict a single-curvature moisture distribution pattern and are associated with a large error in the near-surface region. In this study's SAR imaging results, it was found that the double-curvature moisture distribution pattern is very similar to the SAR amplitude distribution in Fig. 7, suggesting a promising potential of SAR imaging for subsurface moisture distribution sensing of concrete specimens and structures.

Conclusion

Moisture characterization inside concrete using a nondestructive approach is an important and challenging problem for the durability of concrete structures. In this experimental work using SAR imaging for subsurface moisture characterization, it was found that higher SAR amplitudes indicate stronger electromagnetic scattering response, suggesting greater values of dielectric constant (real part of relative complex electric permittivity). The increase in the dielectric constant of wet concrete is attributed to the presence of moisture inside the porous structure of theconcrete. Meanwhile, with the increase of moisture content, higher SAR amplitudes also exhibit broader spatial distribution in SAR images. This result is due to the capability of SAR imaging to project scattered radar signals back to their estimated spatial locations. The spatial distribution of SAR amplitudes shows insightful information for subsurface sensing and can be used to relate to moisture distribution inside a concrete panel specimen. The use of critical contours in SAR images is proposed for both qualitatively correlating with moisture distribution and quantitatively estimating moisture content inside a concrete penal specimen in this research. A procedure summarizing the steps for determining critical contour from SAR images has also been presented. From this result, the promising potential of SAR imaging for moisture characterization inside concrete has been demonstrated.

References

Akita, H., T. Fujiwara, and Y. Ozaka. 1997. "A practical procedure for the analysis of moisture transfer within concrete due to drying." *Mag. Concr. Res.* 49 (179): 129–137. https://doi.org/10.1680/macr.1997.49.179.129.

Amba, J. C., J. P. Balayssac, and C. H. Détriché. 2010. "Characterization of differential shrinkage of bonded mortar overlays subjected to drying." *Mater. Struct.* 43 (1–2): 297–308. https://doi.org/10.1617/s11527-009-9489-8.

Bentur, A., S. Diamond, and N. S. Berke. 1997. *Steel corrosion in concrete*. London: E & FN Spon.

Cai, H., and X. Liu. 1998. "Freeze-thaw durability of concrete: Ice formation process in pores." *Cem. Concr. Res.* 28 (9): 1281–1287. https://doi.org/10.1016/S0008-8846(98)00103-3.

Cano-Barrita, P. D. J., B. J. Balcom, T. W. Bremner, M. B. MacMillan, and W. S. Langley. 2004. "Moisture distribution in drying ordinary and high performance concrete cured in a simulated hot dry climate." *Mater. Struct.* 37 (8): 522–531. https://doi.org/10.1007/BF02481576.

Chen, D., and A. Wimsatt. 2010. "Inspection and condition assessment using ground penetrating radar." *J. Geotech. Environ. Eng.* 136 (1): 207–214. https://doi.org/10.1061/(ASCE)GT.1943-5606.0000190.

Cornell, J. B., and A. T. Coote. 1972. "The application of an infrared absorption technique to the measurement of moisture content of building materials." *J. Appl. Chem. Biotechnol.* 22 (4): 455–463. https://doi.org/10.1002/jctb.2720220403.

Fagerlund, G. 1977. "The critical degree of saturation method of assessing the freeze/thaw resistance of concrete." *Mater. Struct.* 10 (4): 217–229. https://doi.org/10.1007/BF02478694.

Garbalinska, H., M. Stasiak, M. Bochenek, and G. Musielak. 2018. "Assessment of a new method for determining the relationship between effective diffusivity and moisture concentration—Exemplified by autoclaved aerated concrete of four density classes." *Int. J. Heat Mass Transfer* 124: 288–297. https://doi.org/10.1016/j.ijheatmasstransfer.2018.03.051.

Gonzalez, J. A., W. Lopez, and P. Rodriguez. 1993. "Effects of moisture availability on corrosion kinetics of steel embedded in concrete." *Corrosion* 49 (12): 1004–1010.

Kim, J.-K., and C.-S. Lee. 1999. "Moisture distribution of concrete considering self-desiccation at early ages." *Cem. Concr. Res.* 29 (12): 1921–1927. https://doi.org/10.1016/S0008-8846(99)00192-1.

Klysz, G., and J. P. Balayssac. 2007. "Determination of volumetric water content of concrete using ground-penetrating radar." *Cem. Concr. Res.* 37 (8): 1164–1171. https://doi.org/10.1016/j.cemconres.2007.04.010.

Kong, J. A. 2000. *Electromagnetic wave theory*. Cambridge, MA: EMW.

Laurens, S., J. P. Balayssac, J. Rhazi, and G. Arliguie. 2002. "Influence of concrete relative humidity on the amplitude of ground-penetrating radar (GPR) signal." *Mater. Struct.* 35 (4): 198–203. https://doi.org/10.1007/BF02533080.

Laurens, S., J. P. Balayssac, J. Rhazi, and G. Arliguie. 2005. "Non-destructive evaluation of concrete moisture by GPR experimental study and direct modeling." *Mater. Struct.* 38 (9): 827–832. https://doi.org/10.1617/14295.

Li, K., C. Li, and Z. Chen. 2009. "Influential depth of moisture transport in concrete subject to drying-wetting cycles." *Cem. Concr. Compos.* 31 (10): 693–698. https://doi.org/10.1016/j.cemconcomp.2009.08.006.

Multon, S., E. Merliot, M. Joly, and F. Toutlemonde. 2004. "Water distribution in beams damaged by alkali-silica reaction: Global weighing and local gammadensitometry." *Mater. Struct.* 37 (5): 282–288. https://doi.org/10.1007/BF02481673.

Popovic, S. 2005. "Effects of uneven moisture distribution on the strength of and wave velocity in concrete." *Ultrasonics* 43 (6): 429–434. https://doi.org/10.1016/j.ultras.2004.09.007.

Quincot, G., M. Azenha, J. Barros, and R. Faria. 2011. *State of the art–Methods to measure moisture in concrete*. Portugal: Projetos De Investigação Científica E Desenvolvimento Tecnológico.

Sánchez, I., C. Antón, G. Vera, J. M. Ortega, and M. A. Climent. 2013. "Moisture distribution in partially saturated concrete studied by impedance spectroscopy." *J. Nondestr. Eval.* 32 (4): 362–371. https://doi.org/10.1007/s10921-013-0190-z.

Sbartaï, Z. M., S. Laurens, J. P. Balayssac, G. Ballivy, and G. Arliguie. 2006. "Effect of concrete moisture on radar signal amplitude." *ACI Mater. J.* 103 (6): 419–426.

Sbartaï, Z. M., S. Laurens, and D. Breysse. 2009. "Concrete moisture assessment using radar NDT technique–comparison between time and frequency domain analysis." In *Proc., Non-Destructive Testing in Civil Engineering*. Nantes, France.

Sbartaï, Z. M., S. Laurens, J. Rhazi, J. P. Balayssac, and G. Arliguie. 2007. "Using radar direct wave for concrete condition assessment: Correlation with electrical resistivity." *J. Appl. Geophys.* 62 (4): 361–374. https://doi.org/10.1016/j.jappgeo.2007.02.003.

Šelih, J., C. S. Antonio, and W. B. Theodore. 1996. "Moisture transport in initially fully saturated concrete during drying." *Transp. Porous Media* 24 (1): 81–106. https://doi.org/10.1007/BF00175604.

Downloaded from ascelibrary.org by Tzuyang Yu on 09/11/18. Copyright ASCE. For personal use only; all rights reserved.

Senin, S. F., and R. Hamid. 2016. "Ground penetrating radar wave attenuation models for estimation of moisture and chloride content in concrete slab." *Constr. Build. Mater.* 106 (1): 659–669. https://doi.org/10.1016/j.conbuildmat.2015.12.156.

Shoukry, S. N., G. W. William, B. Downie, and M. Y. Riad. 2011. "Effect of moisture and temperature on the mechanical properties of concrete." *Constr. Build. Mater.* 25 (2): 688–696. https://doi.org/10.1016/j.conbuildmat.2010.07.020.

Stark, D. 1991. "The moisture condition of field concrete exhibiting Alkali-Silica reactivity." In Vol. 126 of *Proc., CANMET/ACI Second Int. Conf. on Durability of Concrete*, 973–987. Farmington Hills, MI: American Concrete Institute.

Tsang, L., J. A. Kong, and K.-H. Ding. 2000. *Scattering of electromagnetic waves—Theories and applications*. New York: Wiley.

Wang, Z., Q. Zeng, L. Wang, Y. Yao, and K. Li. 2014. "Effect of moisture content on freeze-thaw behavior of cement paste by electrical resistance measurements." *J. Mater. Sci.* 49 (12): 4305–4314. https://doi.org/10.1007/s10853-014-8126-2.

Ye, T., J. Nanguo, and J. Xianyu. 2018. "Coupling effect of temperature and relative humidity diffusion in concrete under ambient conditions." *Constr. Build. Mater.* 159 (20): 673–689. https://doi.org/10.1016/j.conbuildmat.2017.10.128.

Yu, T. Y. 2010. *Damage detection of GFRP-concrete systems using electromagnetic waves–Theory and experiment*. Cologne, Germany: LAP LAMBERT.

Yu, T. Y. 2011. "Distant damage-assessment method for multilayer composite systems using electromagnetic waves." *J. Eng. Mech.* 137 (8): 547–560. https://doi.org/10.1061/(ASCE)EM.1943-7889.0000257.

Yu, T. Y. 2017. "Quantitative assessment of CFRP-concrete cylinders using synthetic aperture radar images." *Res. Nondestr. Eval.* 28 (3): 168–185. https://doi.org/10.1080/09349847.2016.1173266.

Zeng, Q., T. Fen-Chong, P. Dangla, and K. Li. 2011. "A study of freezing behavior of cementitious materials by poromechanical approach." *Int. J. Solids Struct.* 48 (22): 3267–3273. https://doi.org/10.1016/j.ijsolstr.2011.07.018.

Zhang, J., K. Qi, and Y. Huang. 2009. "Calculation of moisture distribution in early-age concrete." *J. Eng. Mech.* 135 (8): 871–880. https://doi.org/10.1061/(ASCE)0733-9399(2009)135:8(871).

Downloaded from ascelibrary.org by Tzuyang Yu on 09/11/18. Copyright ASCE. For personal use only; all rights reserved.